

Improving Forecasting Ability of GITM using Data-driven Model Refinement

Brandon M. Ponder¹, Aaron J. Ridley², Ankit Goel³, and Dennis S. Bernstein²

¹University of Michigan

²University of Michigan-Ann Arbor

³University of Maryland

November 21, 2022

Abstract

At altitudes below about 600 km, satellite drag is one of the most important and variable forces acting on a satellite. Neutral mass density predictions in the upper atmosphere are therefore critical for (1) designing satellites; (2) performing adjustments to stay in an intended orbit; and (3) collision avoidance maneuver planning. Density predictions have a great deal of uncertainty, including model biases and model misrepresentation of the atmospheric response to energy input. These may stem from inaccurate approximations of terms in the Navier-Stokes equations, unmodeled physics, incorrect boundary conditions, or incorrect parameterizations. Two commonly parameterized source terms are the thermal conduction and eddy diffusion. Both are critical components in the transfer of the heat in the thermosphere. Determining how well the major constituents (N₂, O₂, O) are as heat conductors will have effects on the temperature and mass density changes from a heat source. This work shows the effectiveness of using the retrospective cost model refinement (RCMR) technique at removing model bias caused by different sources within the Global Ionosphere Thermosphere Model (GITM). Numerical experiments, Challenging Minisatellite Payload (CHAMP) and Gravity Recovery and Climate Experiment (GRACE) data during real events are used to show that RCMR can compensate for model bias caused by both inaccurate parameterizations and drivers. RCMR is used to show that eliminating model bias before a storm allows for more accurate predictions throughout the storm.

1 **Improving Forecasting Ability of GITM using Data-driven**
2 **Model Refinement**

3 **¹Brandon M. Ponder, ¹Aaron J. Ridley, ²Ankit Goel, ³D. S. Bernstein**

4 ¹Department of Climate and Space Sciences and Engineering, University of Michigan, Ann Arbor, MI USA

5 ²Department of Mechanical Engineering, University of Maryland, Baltimore County, Baltimore, MD USA

6 ³Department of Aerospace Engineering, University of Michigan, Ann Arbor, MI USA

Corresponding author: B. M. Ponder, bponder@umich.edu

Abstract

At altitudes below about 600 km, satellite drag is one of the most important and variable forces acting on a satellite. Neutral mass density predictions in the upper atmosphere are therefore critical for (1) designing satellites; (2) performing adjustments to stay in an intended orbit; and (3) collision avoidance maneuver planning. Density predictions have a great deal of uncertainty, including model biases and model misrepresentation of the atmospheric response to energy input. These may stem from inaccurate approximations of terms in the Navier-Stokes equations, unmodeled physics, incorrect boundary conditions, or incorrect parameterizations. Two commonly parameterized source terms are the thermal conduction and eddy diffusion. Both are critical components in the transfer of the heat in the thermosphere. Determining how well the major constituents (N_2 , O_2 , O) are as heat conductors will have effects on the temperature and mass density changes from a heat source. This work shows the effectiveness of using the retrospective cost model refinement (RCMR) technique at removing model bias caused by different sources within the Global Ionosphere Thermosphere Model (GITM). Numerical experiments, Challenging Minisatellite Payload (CHAMP) and Gravity Recovery and Climate Experiment (GRACE) data during real events are used to show that RCMR can compensate for model bias caused by both inaccurate parameterizations and drivers. RCMR is used to show that eliminating model bias before a storm allows for more accurate predictions throughout the storm.

1 Introduction

Orbit estimation of drag along a satellite path for collision avoidance is growing in importance due to the increased risk of collisions as more objects are being launched into low Earth orbit. Satellites are expensive to build, launch and maintain [Saleh *et al.*, 2004] and there is an increasing collision risk posed by over twenty thousand pieces of space debris larger than 10 cm^3 [Garcia, 2021]. In response to the threat of collisions, the Joint Space Operations Center (JSpOC) continuously monitors orbiting objects' positions and velocities. From its database, it computes a probability of collision between two bodies and will issue a Conjunction Data Message (CDM) to the mission operator for further action [Hejduk and Frigm, 2015], [Bussy-Virat *et al.*, 2018]. Then a collision avoidance maneuver could be performed, costing time of inactivity and fuel.

There are underlying assumptions to the advanced computing technique of predicting a collision. One assumption is the drag force estimation used to solve the kinematic

equations. The acceleration (\underline{a}) experienced due to satellite drag is proportional to the ratio of surface area (A) to mass (m) of the spacecraft, coefficient of drag (c_D), the atmospheric density (ρ) and the velocity, relative to a rotating atmosphere, squared (v):

$$\underline{a} = -\frac{1}{2} \frac{A}{m} c_D \rho v^2 \hat{v} \quad (1)$$

37 where density is the largest uncertainty in this equation.

38 Attitude control is a related topic that requires properly estimating the drag-induced
39 torques on a satellite to control its orientation. This could be important for instrumentation
40 to function properly. Part of the attitude control problem is bounding torques to ensure
41 systems do not get overwhelmed. Alternatively, over-engineering a powerful attitude con-
42 trol system costs extra money. The accuracy of torque prediction is reliant on low-error
43 density estimation too. *Moorthy et al.* [2021] describes the importance of attitude control
44 and the potential impact to expand our ability to explore extremely low Earth orbits (150-
45 250 km). This region of Earth's atmosphere is under-explored due to the large drag force
46 causing short expected lifetimes.

47 Accurately predicting the density in the thermosphere is a difficult task and atmo-
48 spheric models are often called upon to make these density-driven drag estimations, but
49 can be inaccurate by 20% ([*Kuang et al.*, 2014], [*Marcos*, 1990], [*Bruinsma et al.*, 2004]).
50 The errors in the prediction are amplified during a geomagnetic storm, largely due to poor
51 density estimation [*Pachura and Hejduk*, 2016]. Drag inaccuracies can create positioning
52 errors on the order of 10 km after just one day. In a short period of time, the satellites'
53 trajectory can change enough such that JSpOC may need to reacquire them.

54 One of the models available to estimate density is NRLMSISE-00 (referred to as
55 MSIS). MSIS is an empirical model ([*Hedin*, 1983], [*Hedin*, 1987], [*Hedin*, 1991], [*Pi-*
56 *cone et al.*, 2002]) that uses a spherical harmonic fitting of ground-based and satellite
57 measurements to estimate neutral densities and temperatures of the thermosphere for given
58 solar conditions (F10.7) and geomagnetic activity (A_p). Empirical models incorporate
59 data from remote observations so they are able to capture background neutral densities
60 well, but do not have the same success during a solar storm due to limited time periods
61 of enhanced activity. *Wang et al.* [2022] analyzed 265 storms, showed that MSIS under-
62 predicted the density during storms, and fit coefficients to improve MSIS's peak density
63 prediction during weak, moderate and intense storms.

64 The Jacchia-Bowman 2008 Empirical Thermospheric Density Model (JB2008)
65 [*Bowman et al.*, 2008] is an empirical model that estimates total mass density. JB2008
66 is a series of improvements upon the Jacchia 70 model [*Jacchia*, 1970] changing the in-
67 put for the geomagnetic indices (from A_p to D_{st}) and adding to the input for the solar
68 indices using orbit-based sensor measurements of solar data in the EUV and far EUV
69 (FUV) wavelengths. As part of the change from Jacchia 70, *Bowman* [2004] concluded
70 that a Fourier time series and an altitude dependent, quadratic function could accurately
71 replace the existing Jacchia 70 density functions used to compute the semidiurnal density
72 variation. *Bowman et al.* [2006] introduced EUV and FUV solar indices into their temper-
73 ature equation, replacing the standard Jacchia temperature equation. The accumulation of
74 these changes led to lower standard deviation in errors, particularly during solar minimum
75 conditions and during major geomagnetic storms.

76 There are two common issues with models: (1) bias during background conditions
77 where mean densities from the model differ from mean measurements over a period of
78 several days or longer and (2) enhanced errors over periods of a couple of days, driven by
79 space weather events like storms. There are many ways people have tried to address these
80 issues of poor density estimation.

81 The High Accuracy Satellite Drag Model (HASDM) [*Storz et al.*, 2005] is an exten-
82 sion of JB2008 used by the US Space Force Combined Space Operations Center which
83 uses observed drag effects from approximately 75 Earth-orbiting spheres to compute di-
84 urnal and semidiurnal variations to the thermosphere density. *Doornbos et al.* [2008] has
85 done work with two-line element (TLE) data to directly create altitude-dependent multi-
86 plication factors to scale the densities of empirical models. *Brandt et al.* [2020] created
87 the Multifaceted Optimization Algorithm (MOA) which similarly uses TLE data to incre-
88 mentally adjust the drivers for MSIS within the orbital propagator (SpOCK) [*Bussy-Virat*
89 *et al.*, 2018]. MOA adjusts the drivers of MSIS when MSIS has a large bias or misrep-
90 resents a storm to bring SpOCK-predicted orbits in line with TLEs from several small
91 satellites. Lastly, [*Kalafatoglu Eyiguler et al.*, 2019] showed that debiasing a model's back-
92 ground density prior to a storm may lead to improved performance for some models and
93 recommends a few calculations for assessing storm-time performance.

94 Physics-based models estimate the thermosphere state variables using approxima-
95 tions of the Navier-Stokes equations. The idea is that correctly implemented physics could

96 more accurately reproduce typical and highly-variable thermosphere conditions as ob-
 97 served during storms. Coupled Thermosphere Ionosphere Model (CTIM) [Fuller-Rowell
 98 and Rees, 1980], Thermosphere Ionosphere Electrodynamics General Circulation Model
 99 (TIEGCM) [Richmond *et al.*, 1992] and Global Ionosphere Thermosphere Model (GITM)
 100 [Ridley *et al.*, 2006] are examples of Earth-based, physics models. The different numer-
 101 ical approximations, source terms included (or not included), and drivers in each model
 102 generates different temperatures, wind structures and densities. TIEGCM and CTIM use
 103 the hydrostatic assumption, whereas GITM does not make the same hydrostatic equilib-
 104 rium assumption and solves a more complete vertical momentum and energy equation, but
 105 takes significantly longer to run. GITM makes use of the Flare Irradiance Spectral Model
 106 (FISM) [Chamberlin *et al.*, 2008] fluxes to better represent the solar EUV entering the
 107 atmosphere.

108 This study presents work on debiasing the background density in GITM using obser-
 109 vational data. It also shows the impact of debiasing a model prior to a geomagnetic storm
 110 using satellite measurements and the MSIS model.

111 1.1 The Global Ionosphere Thermosphere Model (GITM)

112 Understanding the parameters that affect the thermosphere’s neutral density are
 113 critical for improving physics-based models like GITM. GITM is a 3D spherical model
 114 that is used for Earth [Ridley *et al.*, 2006], Mars [Bougher *et al.*, 2015] and Saturn’s moon
 115 Titan [Bell *et al.*, 2010]. In this study, the resolution of GITM was 2° latitude and 4° in
 116 longitude.

Ridley *et al.* [2006] explains the capabilities of the model, including the chemistry
 and numerical schemes. The vertical energy equation in GITM, including source terms, is
 [Ridley *et al.*, 2006]:

$$\frac{\partial \mathcal{T}}{\partial t} + u_r \frac{\partial \mathcal{T}}{\partial r} + (\gamma - 1) \mathcal{T} \left(\frac{2u_r}{r} + \frac{\partial u_r}{\partial r} \right) = \frac{k}{c_v \rho \bar{m}_n} Q \quad (2)$$

where the first term is the time rate of change for the normalized, neutral temperature,
 $\mathcal{T} = kT/\bar{m}_n$. The second term is the advection of temperature gradients, while the third
 term is the adiabatic heating, which is a result of the divergence of the velocity. This is
 only the vertical component which depends on the vertical velocity, u_r , radius of the
 Earth, r , and the temperature gradient. γ is the adiabatic index that is attached to the

change in energy from the expansion of the gas. On the right-hand side, c_v is the specific heat, k is Boltzmann's constant, ρ is the mass density, and \bar{m}_n is the mean mass of the neutrals. The various source terms are given by:

$$Q = Q_{EUV} + Q_{NO} + Q_O + \frac{\partial}{\partial r}((\kappa_c + \kappa_{eddy}) \frac{\partial T}{\partial r}) + \sum_i n_i m_i \sum_n \frac{\nu_{in} [3k(T_n - T_i) + m_n(v - u)^2]}{m_i + m_n} \quad (3)$$

117 where: Q_{EUV} is the contribution from the solar extreme ultraviolet irradiance; the Q_{NO}
 118 and Q_O terms are the cooling to space from the 5.3 μm and 63 μm bands respectively.
 119 The last term is the collisional frictional heating and heat transfer between ions and neu-
 120 trals. This is a function of the ion density (n_i), mass of the ion (m_i), mass of the neutrals
 121 (m_n), the ion-neutral collision frequency (ν_{in}), the ion velocity (v_i), neutral velocity
 122 (u_n), ion temperature (T_i) and the neutral temperature (T_n). Finally, the fourth term is the
 123 thermal conductivity, where κ_{eddy} and κ_c are the conductivity coefficients due to eddy
 124 diffusion and molecular heat conductivity respectively, and is the focus of this study.

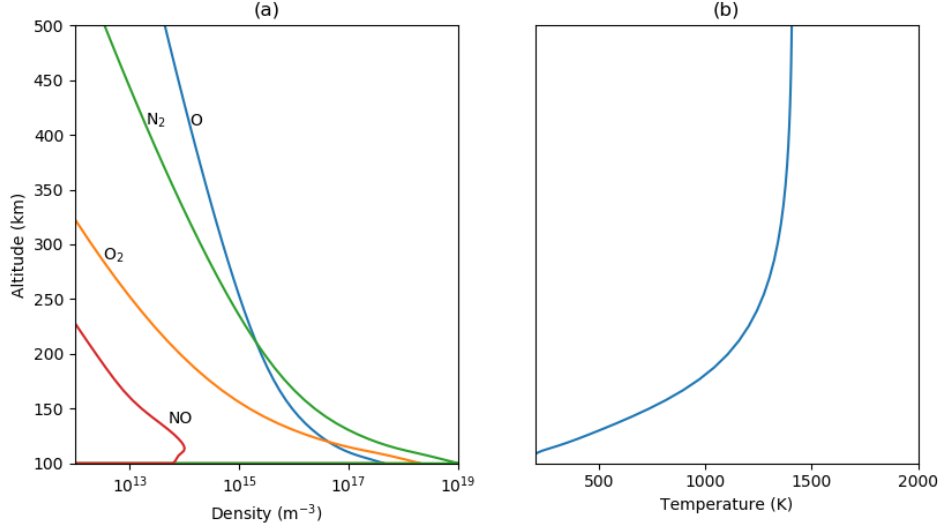
125 1.2 Thermal Conductivity in the Upper Atmosphere

Thermal conductivity uncertainty is a serious issue in physics-based models ([*Banks and Kockarts, 1973*], [*Pawlowski and Ridley, 2009*], [*Schunk and Nagy, 2004*]). Most of the literature describes thermal conductivity in a laboratory setting where it is expressed as a function of temperature alone for specific species [*Vargaftik et al., 1993*]. The theoretical expression for the thermal conductivity coefficient (κ_c) are complex and so it has been useful to simplify the coefficient to be a parameterization ([*Banks and Kockarts, 1973*], [*Schunk and Nagy, 2004*]) as:

$$\kappa_c = \sum_{i=O, O_2, N_2} \left[\frac{N_i}{N_{total}} \right] A_i T^s \quad (4)$$

129 where N_i/N_{total} is a weighting factor by number density of each neutral species, T is
 130 the thermosphere temperature, A_i and s are species specific thermal conductivity coeffi-
 131 cients to fit the total conductivity as needed. The summation includes the three species
 132 with the largest concentrations in the thermosphere. From Figure 1, above about 200 km,
 133 O is a dominant neutral species whereas in the lower thermosphere O_2 and N_2 densities
 134 are more prevalent and must be considered in the contribution to the heat exchange proc-
 135 cess. The temperature profile shows that above about 250 km, the atmosphere is roughly
 136 isothermal, so the conduction term can be quite small. This is the region where O is

137 dominant. This implies that the N_2 term in the thermal conductivity is probably a more
 138 important term since N_2 is dominant below ~ 250 km where the vertical temperature
 139 gradient is largest.



126 **Figure 1.** (a) Globally averaged atmosphere constituents and (b) globally averaged temperature in the ther-
 127 mosphere from GITM on September 26th, 2002. This time period is representative of solar max conditions
 128 ($F_{10.7} \approx 180$) and is used in some of the tests performed in later sections.

Pavlov [2017] gives approximations from tabulated values in *Vargaftik et al.* [1993] for thermal conduction (denoted as λ in *Pavlov* [2017]) experiencing pressures much less than 0.1 MPa in temperature ranges of 160 - 2500 K for N_2 and 160 - 1500 K for O_2 . The full expressions are:

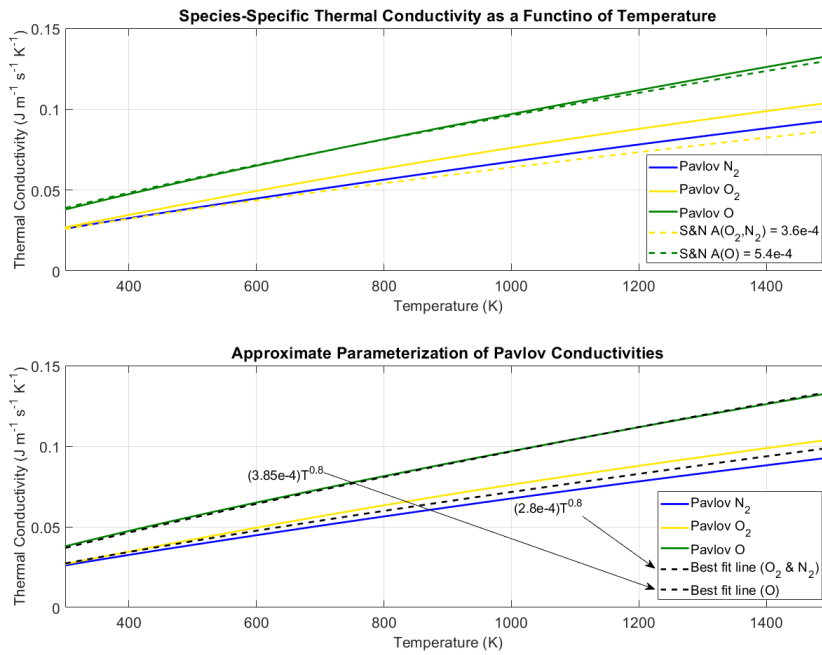
$$\kappa_{N_2} = -3520 + 720.5T^{0.5} - 41.93T + 1.613T^{1.5} - 0.02685T^2 + 1.665 \times 10^{-4}T^{2.5} \quad (5)$$

$$\kappa_{O_2} = -3169 + 735.7T^{0.5} - 53.83T + 2.583T^{1.5} - 0.05325T^2 + 4.083 \times 10^{-4}T^{2.5} \quad (6)$$

$$\kappa_O = 46.7(1 + 2.228 \times 10^{-5}T - 5.545 \times 10^{-9}T^2)T^{0.77} \quad (7)$$

144 Figure 2 shows the *Pavlov* [2017] values of κ_{N_2} , κ_{O_2} , κ_O , as well as the corresponding
 145 *Schunk and Nagy* [2004] conductivities (assuming $s = 0.75$). In the bottom subplot, "best
 146 fit" lines are shown using the same parameterization scheme in (4). The estimation of the

147 coefficients and exponent in the parameterization are derived from data and theoretical
 148 expressions of the thermal conductivity of individual gases from [Hilsenrath, 1960], [Reid
 149 *et al.*, 1977], [Lide, 1997], [Barlier *et al.*, 1969] and [Banks and Kockarts, 1973]. While
 150 Vargafitik *et al.* [1993] describes more complex expressions that best fit to an exponent
 151 close to 0.8. Although the parameterizations of the atomic oxygen, O , and nitrogen, N_2 ,
 152 seem to match fairly well, there is a great deal of discrepancy for the estimation of the
 153 O_2 .



140 **Figure 2.** Different species-specific thermal conductivities plotted as a function of temperature with
 141 differing definitions of the suggested parameterization. Top: Pavlov and Schunk and Nagy parameterized
 142 species-specific conductivities. Bottom: Best fit lines for the Pavlov species-specific curves with the form
 143 $A_i T^s$.

154 As described in Pawlowski and Ridley [2009], model bias can originate from incor-
 155 rectly defined parameters like the thermal conductivity, eddy diffusion, or photoelectron
 156 heating efficiencies. Certain quantities such as the eddy diffusion, and lower boundary
 157 density and temperature affect model bias such that the best modeled physics equations
 158 can still result in inaccurate mass density calculations. It is therefore quite difficult to
 159 identify the cause of data-model comparison discrepancies.

160 For example, *Masutti et al.* [2016] explored a time period in which F10.7 increased
161 over the course of several days and showed that GITM’s mass density at approximately
162 400 km altitude overresponded to this change. Overall, there was an underestimate of
163 a mass density when F10.7 was low and an overestimate when F10.7 was high. Since
164 GITM’s performance was a function of the solar irradiance, improved performance could
165 possibly be captured through thermal conductivity adjustments based on solar activity, but
166 may be possibly masking other incorrectly modeled physics.

167 The thermal conductivity is the focus of this study because its parameterization
168 is a possible deficiency in GITM and it significantly changes the density results needed
169 for orbit prediction. This is an opportunity to settle the discrepancy of parameterizations
170 and compensate for neutral density model bias that may be caused by other incorrectly
171 modeled physics, boundary conditions or drivers. For instance, inaccurate modeling of a
172 term like the eddy diffusion coefficient could also influence neutral density results [*Qian*
173 *et al.*, 2009]. Handling the eddy diffusion has been a topic of previous research in GITM
174 ([*Goel et al.*, 2018], [*Malhotra et al.*, 2017]), but the eddy diffusion is a term that also
175 controls the composition and ionospheric density due to the changed turbulent mixing and
176 its inclusion in the continuity, vertical momentum and energy equations.

177 **1.3 Manually Debiassing the Thermal Conductivity**

178 This section outlines the need for debiasing models by describing an attempt to
179 choose a single constant, thermal conductivity coefficient that allows GITM’s mass density
180 to better match CHAMP observations. Nine runs with varying thermal conductivity coef-
181 ficients (Table 1) were performed for each of six different time periods. For each run, the
182 eddy diffusion coefficient was set to 500, and s was set to 0.69. The percent difference in
183 mass density from CHAMP measurements and GITM calculations were examined. GITM
184 was ran for ten days, but only the last five days of each run were used to allow GITM
185 to reach a quasi-diurnally reproducible state before comparison. CHAMP and GITM
186 densities were averaged over the orbital period (~ 90 minutes).

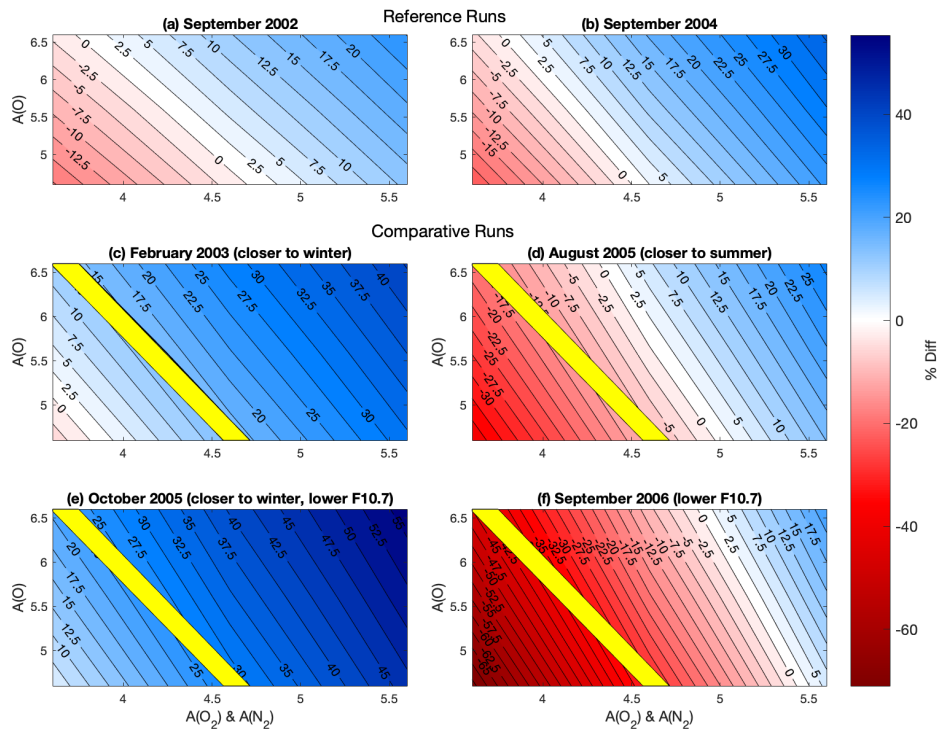
189 Contours of percent error for each time period are shown in Figure 3. The Septem-
190 ber 2002 and September 2004 time periods were selected to tune GITM, keeping the
191 season and geomagnetic conditions similar, but allowing the solar activity to vary (see
192 Table 2).

Run	A(O ₂ , N ₂)	A(O)
1	3.6	4.6
2	4.6	4.6
3	5.6	4.6
4	3.6	5.6
5	4.6	5.6
6	5.6	5.6
7	3.6	6.6
8	4.6	6.6
9	5.6	6.6

187 **Table 1.** The variety of inputs to thermal conductivity coefficients. Multiply $A(i)$ by 10^{-4} to yield
 188 $Jm^{-1}s^{-1}K^{-1}$.

Time period	F10.7
September 2002	184
February 2003	133
September 2004	92
August 2005	94
October 2005	80
September 2006	74

193 **Table 2.** F10.7 (solar flux units) values during the different time periods.



194 **Figure 3.** Contours of model errors as a function of thermal conductivity (molecular on x-axis, atomic on
 195 y-axis) for different time periods. The blue and red regions indicate GITM having mass densities lower and
 196 higher than CHAMP observed, respectively. Areas of white yield results similar mean densities to CHAMP.
 197 (a) and (b) are baseline runs to find suitable thermal conductivity coefficients. The yellow region in (c)-(f) are
 198 thermal conduction values that yield good results for both the reference runs to within 5%.

199 As the thermal conductivity is increased, the gradient in temperature in the lower
 200 thermosphere decreases. Since the lower boundary condition fixes the temperature, the
 201 temperature in the upper thermosphere must decrease. Pressure and density profiles are
 202 strongly controlled by the temperature, so as the temperature decreases, the density at
 203 a fixed altitude in the upper thermosphere also decreases. This means that the neutral
 204 density in GITM decreases as the thermal conductivity increases. Figure 3 shows that
 205 the molecular coefficient has a stronger effect than the atomic oxygen coefficient. This
 206 is because the thermal conductivity multiplies ∇T , which is largest in the lower ther-
 207 mosphere (~ 100 - 200 km), where the major species O_2 and N_2 are dominant (Figure 1).

208 Hence, the thermal conductivity in the lower thermosphere dictates the middle and upper
209 thermosphere temperature and density.

210 The top two plots of Figure 3 indicate that, for these two intervals, there is a span
211 of atomic and molecular coefficients that reduce the model bias to extremely low levels,
212 even with different solar irradiance. However, when the study was expanded to include
213 other seasons and other conditions, it became clear that no combination reduced the bias
214 universally. Times outside of September 2002 and 2004 needed to be considered to see
215 that this overlapping parameterization space does not provide unbiased results at different
216 parts of the solar cycle. The yellow zone overlaid on each subplot is the parameter space
217 from the September 2002 and 2004 runs where the error was within $\pm 5\%$ for both times.
218 These yellow zones show that a debiased set of thermal conductivity parameters for one
219 set of times do not necessarily reduce the error to zero for other time periods. The causes
220 of this could stem from incorrect drivers (EUV, lower boundary condition, aurora, etc...)
221 or incorrect physics (ion variability, small-scale structures, turbulent heating, etc...). This
222 is the reason an automated debiasing mechanism is needed. The difference in performance
223 to estimate other state variables (aside from the neutral density) between these two sets of
224 thermal conductivity candidates was not studied in this work.

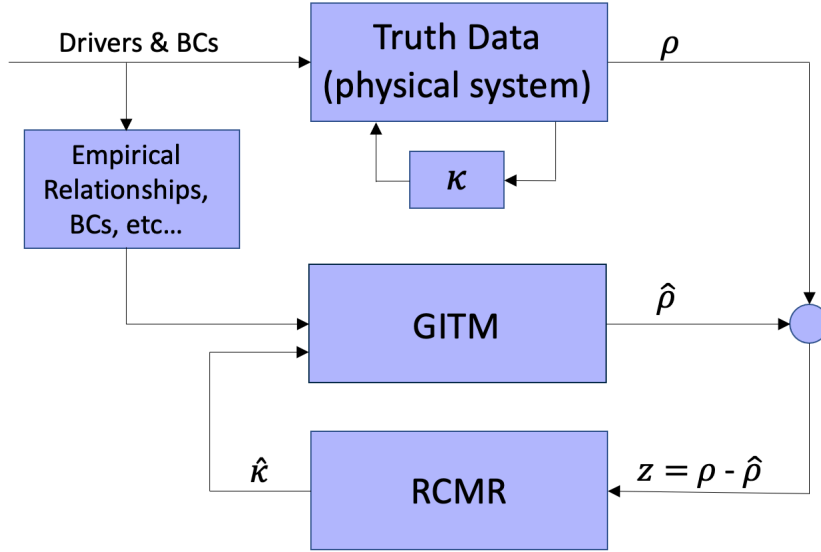
225 **2 Retrospective Cost Model Refinement (RCMR)**

226 Retrospective Cost Model Refinement (RCMR) is a technique developed for param-
227 eter estimation in nonlinear systems [Morozov *et al.*, 2011]. The technique is a variation
228 of retrospective cost adaptive control (RCAC) that was primarily developed for adap-
229 tive control applications in aerospace engineering [Santillo and Bernstein, 2010]. In this
230 work, RCMR is used to estimate thermal conductivity coefficients in a system modeled
231 by Navier-Stokes partial differential equations. RCMR minimizes a cumulative cost func-
232 tion that is based on the difference between the density computed self-consistently by
233 GITM and the density specified externally, such as that measured by a real satellite or
234 estimated by a different model. This technique has been applied for estimation of (1) the
235 eddy diffusion coefficient using total electron content (TEC) as the comparison variable
236 [Goel *et al.*, 2018], (2) NO_x cooling using simulated space-based measurements [D'Amato
237 *et al.*, 2013], (3) the photoelectron heating coefficient based on real satellite measurements
238 [Burrell *et al.*, 2015] and, (4) the thermal conductivity coefficients using simulated density
239 measurements [Goel *et al.*, 2020]. Each of these studies successfully estimated the corre-

240 sponding unknown parameter using RCMR. For a more complete description of RCMR,
241 refer to *Goel et al.* [2020].

242 Figure 4 shows the block diagram used to estimate the unknown parameter within
243 RCMR. As shown by the top block in Figure 4, the external drivers, including the solar
244 EUV, frictional heating and auroral precipitation, force the real thermosphere's density,
245 ρ . Thermal conductivity serves to move the energy vertically. When trying to reproduce
246 nature's physics with a model (GITM), there are assumptions that try to emulate the true
247 relationships. The empirical formulations, boundary conditions and other model necessities
248 result in error accumulation. This is seen when comparing the model estimated density, $\hat{\rho}$
249 with in-situ measurements, as shown in Figure 3.

250 Reducing the error (z) is ideally done by correctly implementing equations that
251 accurately and completely capture all dynamics, boundary conditions and drivers within
252 the model. Low error could also be obtained by incorrect physics within the models that
253 cancel each other out, inadvertently matching the measurements. This can occur when
254 multiple incomplete physics terms compensate for each other. For example, having too
255 low solar EUV heating along with too high frictional heating at high-latitudes could result
256 in an orbit-averaged mass density that is more or less correct. In the case of RCMR,
257 intentionally adjusting thermal conductivity coefficient(s) changes the error by altering the
258 thermal balance between sources and sinks.



259 **Figure 4.** Modified block diagram from *Goel et al.* [2020] to illustrate the RCMR process.

260 In Figure 4, the top block represents the true physical system with real drivers and
 261 boundary conditions. In the real system, κ is driven by the states and dynamics, making
 262 a complex, nonlinear system. GITM approximates the drivers and boundary conditions as
 263 well as approximating the dependence of κ on the system state as described above (i.e. κ
 264 $= \sum A_i T^s$). RCMR takes the difference between the "actual" ρ and the GITM-estimated
 265 $\hat{\rho}$, and alters the κ (through the values of A_i and/or s) to minimize the difference.

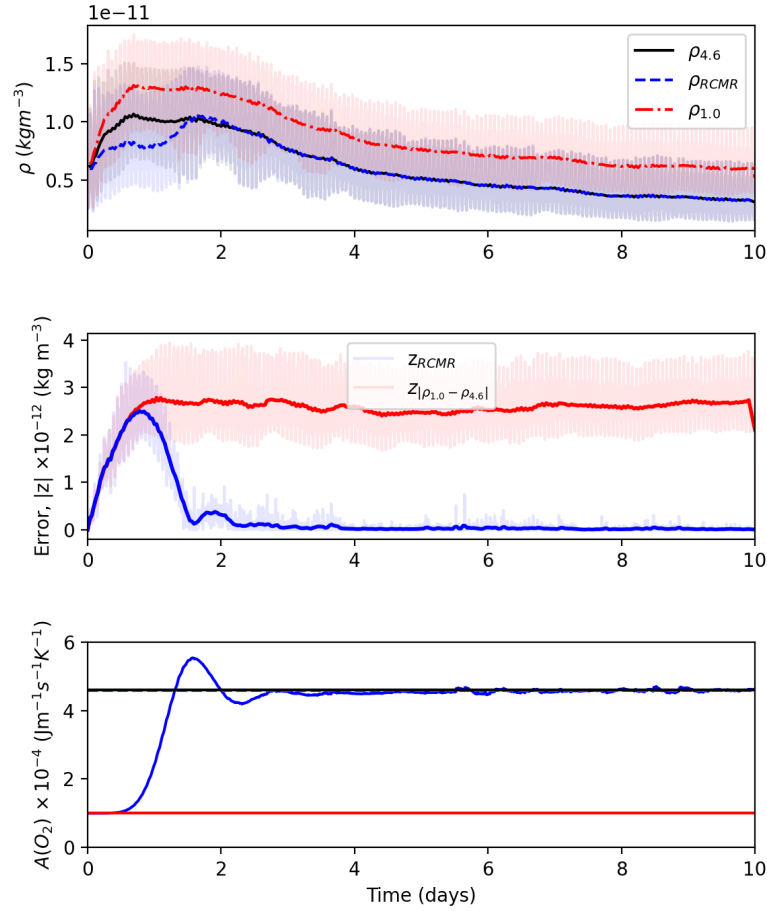
266 In order to validate the integration of RCMR within GITM, RCMR was used to esti-
 267 mate κ ($A(O_2, N_2)$) using simulated truth density data obtained from a GITM simulation
 268 with a known value of κ . The density data was recorded and serves as the satellite mea-
 269 surements. Next, GITM was re-run with an intentionally incorrect $A(O_2, N_2)$ and RCMR
 270 updated the estimate $A(O_2, N_2)$ using the simulated truth density data. If RCMR was
 271 implemented correctly, RCMR's estimated $A(O_2, N_2)$ would converge to the true value of
 272 $A(O_2, N_2)$ used to generate the simulated truth data, validating the technique. When this
 273 is true, it is a good indication that when actual truth data (i.e. CHAMP, GRACE, MSIS) is
 274 used, the convergence will provide the real thermosphere thermal conductivity coefficients.

3 Results

3.1 Automating the Model Debiasing Process via RCMR

RCMR estimates the thermal conductivity coefficients using density measurements from the CHAMP and GRACE satellites as well as Naval Research Laboratory's (NRL) Mass Spectrometer and Incoherent Scatter Radar (MSIS) empirical model [Picone *et al.*, 2002]. In order to implement this, GITM was ran independent of RCMR to obtain global density values from September 16-26, 2002. The thermal conductivity coefficients of $A(O) = 4.6 \times 10^{-4} \text{ Jm}^{-1}\text{s}^{-1}\text{K}^{-1}$, $A(O_2, N_2) = 4.6 \times 10^{-4} \text{ Jm}^{-1}\text{s}^{-1}\text{K}^{-1}$ and the exponent $s = 0.69$ were used. In comparison to CHAMP satellite data, this provided a low-biased mass density result (Figure 3a).

The orbit of the CHAMP satellite was used to extract densities from the GITM run ($\rho_{4,6}$) at a one minute cadence. Using GITM densities at the satellite-position as inputs for RCMR (see Figure 5), a GITM simulation was run again during the same time, but used RCMR to change the molecular coefficient. This was different from Goel *et al.* [2020] which used the global maximum, minimum and mean densities. The thermal conductivity coefficient $A(O_2, N_2)$ was initialized to $1.0 \times 10^{-4} \text{ Jm}^{-1}\text{s}^{-1}\text{K}^{-1}$, while the $A(O)$ and exponent S were held constant at their previously set values above. The densities modeled by GITM with RCMR is denoted as ρ_{RCMR} . RCMR used the $\rho_{4,6}$ data and ρ_{RCMR} data to compute an error (z) to update the thermal conductivity estimation while the simulation progressed. Figure 5 shows that the dynamic adjustments of $A(O_2, N_2)$ in RCMR work, in that the error z decreased to zero, while $A(O_2, N_2)$ converged to $4.6 \text{ Jm}^{-1}\text{s}^{-1}\text{K}^{-1}$ after around three days.

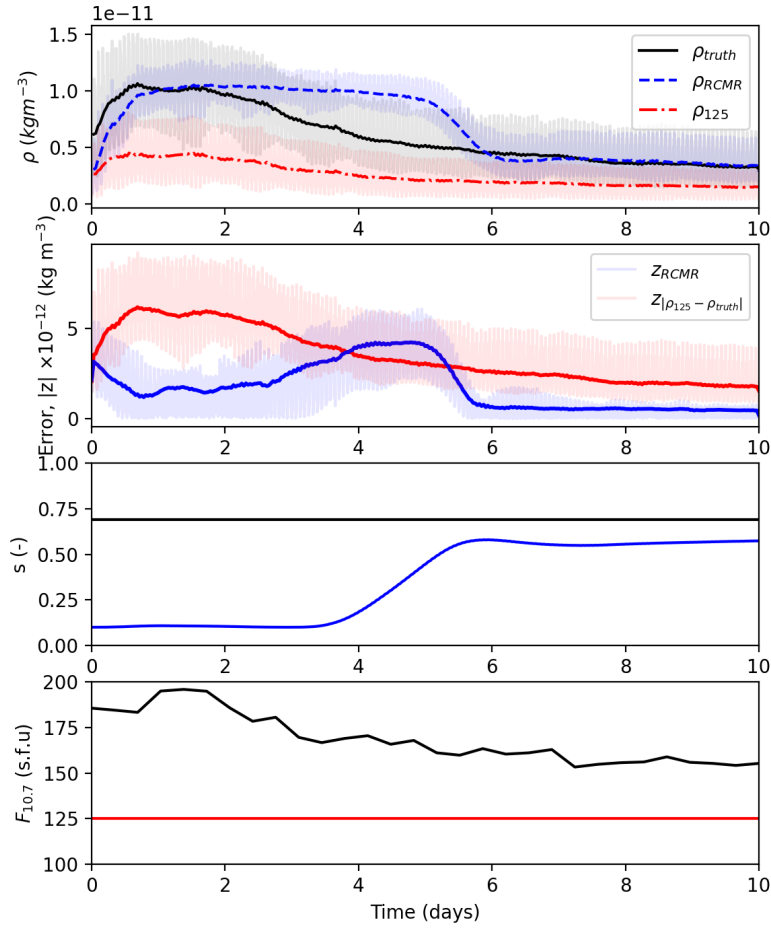


285 **Figure 5.** Top: Densities along the CHAMP orbit are shown with three different values of A_{O_2} . Raw
 286 values are shown as transparent lines, while orbit averaged values are shown as bold. The error (middle)
 287 and thermal conductivity coefficient (bottom) from using simulation data at CHAMP locations at a one
 288 minute cadence is shown in blue for the RCMR assisted run, red for a constant parameterization of $1.0e-4$
 289 $Jm^{-1}s^{-1}K^{-1}$, and black for a constant parameterization of $4.6e-4 Jm^{-1}s^{-1}K^{-1}$. The orbit averaged errors
 290 are shown with a thicker line of their corresponding color.

303 In addition to the truth data and RCMR-adjusted mass densities, the density and
 304 error is shown when the incorrect parameterization was used and not corrected. This
 305 provides a quantification of the level of improvement that can be gained using RCMR.

306 This example shows that RCMR can correct for an incorrectly set thermal coef-
307 ficient, but model bias can be caused by a variety of issues, as described above. For a
308 second example of idealized RCMR runs, illustrated in Figure 6, GITM was run with
309 consistent thermal conductivity parameters but incorrect drivers.

315 F10.7, the daily solar flux at wavelength 10.7 cm, is a proxy for solar spectra
316 [*Richards et al.*, 1994]. An alternative to the F10.7 proxy is using FISM to describe
317 the spectrum [*Chamberlin et al.*, 2008], [*Chamberlin et al.*, 2020]. Near real time and for
318 predictions, F10.7 is approximate and one of the only ways to describe the solar spectrum.
319 If F10.7 is not right or does not describe the spectrum correctly, model bias could result.
320 This second test explores whether RCMR can compensate for an incorrect specification of
321 the F10.7. The RCMR estimated parameter for this run and future runs was the exponent
322 s , with an initial value of s as 0.1.



310 **Figure 6.** Densities and errors are shown with three different run conditions: (1) the truth data used as input
 311 for RCMR in black, (2) the RCMR run dynamically debiasing GITM with incorrect solar drivers in blue, and
 312 (3) the case where GITM has incorrect solar drivers and is not implementing RCMR in red. The orbit aver-
 313 aged errors are shown with a thicker line of their corresponding color. The third subplot shows the thermal
 314 conductivity exponent over time. The bottom subplot shows the corresponding F10.7 used in each run.

323 Similarly to the previous run, the truth data being used was an extraction of GITM
 324 results where the F10.7 was updated based on the actual F10.7, which varied from 190
 325 to 150 solar flux units. The RCMR run was intentionally run with an incorrect constant
 326 F10.7 of 125 solar flux units. Over time, the RCMR-debiased run converged to the truth
 327 data and the error decreased dramatically. The time it took to converge was longer than

Satellite	Sept. 2002 Altitude (km)	Sept. 2004 Altitude (km)	Inclination (°)
CHAMP	390-450	370-410	87.3
GRACE	485-515	460-505	89.0

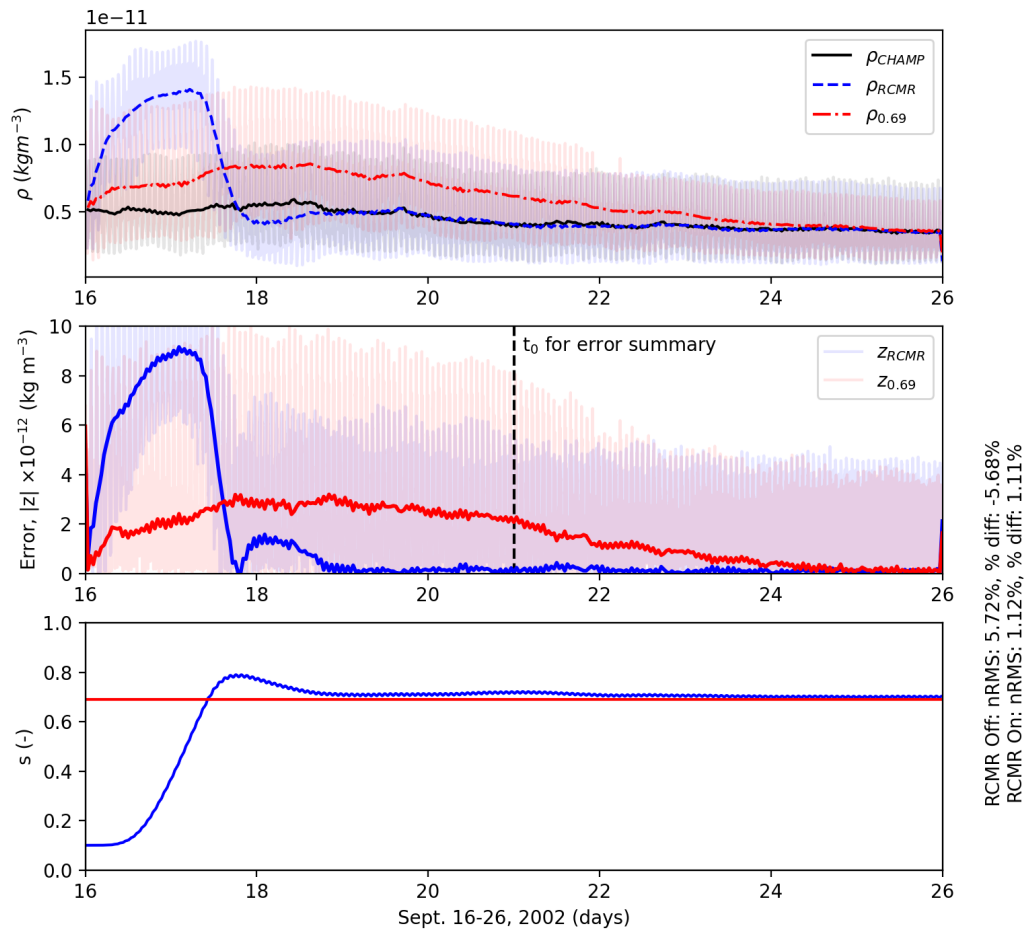
343 **Table 3.** Information on the altitude and orbit inclination during the two test periods.

328 the first test by roughly two days. This was due to the densities being similar between
329 the two runs for the first two days despite the very different run settings. In this case,
330 a low F10.7 incorrect driver caused a low density, having a negative bias. At the same
331 time, a low initial value of s caused a high density since the thermal conduction would be
332 reduced leading to a high temperature. In this case, a positive bias would result. In combi-
333 nation, the biases mostly cancelled and RCMR was relatively ineffective for the first two
334 days. After this, RCMR was able to track the error and produced an 's' that adequately
335 compensated for the incorrect specification of F10.7.

336 **3.2 RCMR with CHAMP and GRACE Satellite Densities**

337 In the previous section, the simulated densities generated from a GITM run repre-
338 sented the "true" thermosphere. In this section, tests of RCMR with real satellite data are
339 described. Initial tests were done using data from September of the years 2002 and 2004
340 as sample months for high and moderate F10.7 fluxes, respectively, since these were used
341 for manual debiasing earlier in the study. Both time periods had relatively low levels of
342 activity, with $|D_{st}|$ being less than 50 nT during each time period.

344 The estimation of the thermal conductivity exponent s was explored using CHAMP
345 and GRACE individually. Figures 7 and 8 show the September 16-26, 2002 period com-
346 paring the results of GITM with a constant thermal conductivity to the RCMR adjusted
347 values against the satellite observations.

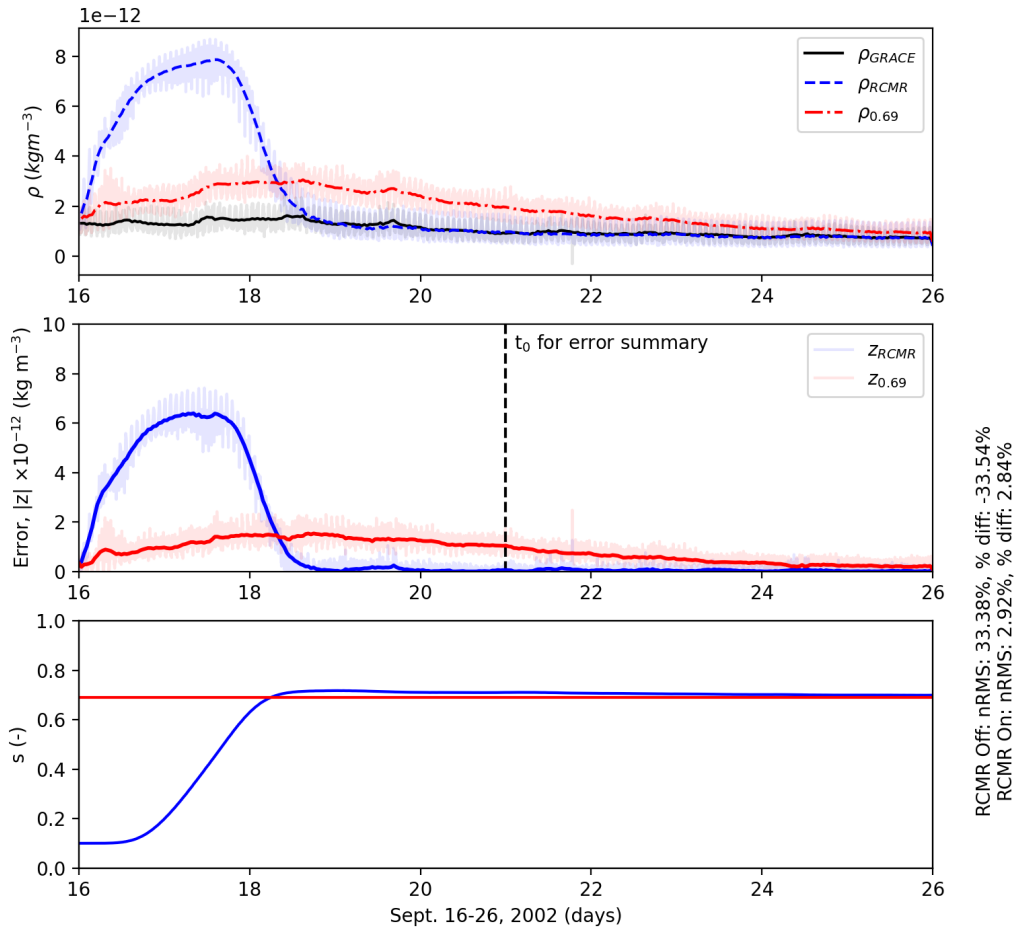


348 **Figure 7.** The top subplot shows the raw and orbit averaged densities are shown for GITM, CHAMP and
 349 RCMR. In the middle subplot, the errors are plotted over one another to observe how RCMR compares to
 350 a constant thermal conductivity typically used in GITM. The bottom subplot shows the consequent thermal
 351 conductivity exponent estimated in blue. In red is the constant value used when RCMR was not applied. The
 352 local time of ascending node for CHAMP was 13.4 LT.

353 The RCMR and non-RCMR runs both converge to the CHAMP and GRACE mea-
 354 surements. With RCMR, the convergence is much faster with large improvements in mass
 355 density after around two to three days. As observed in Figures 7 and 8, the free parameter
 356 s converged to 0.70 which is similar to the constant value of 0.69 used in a typical GITM

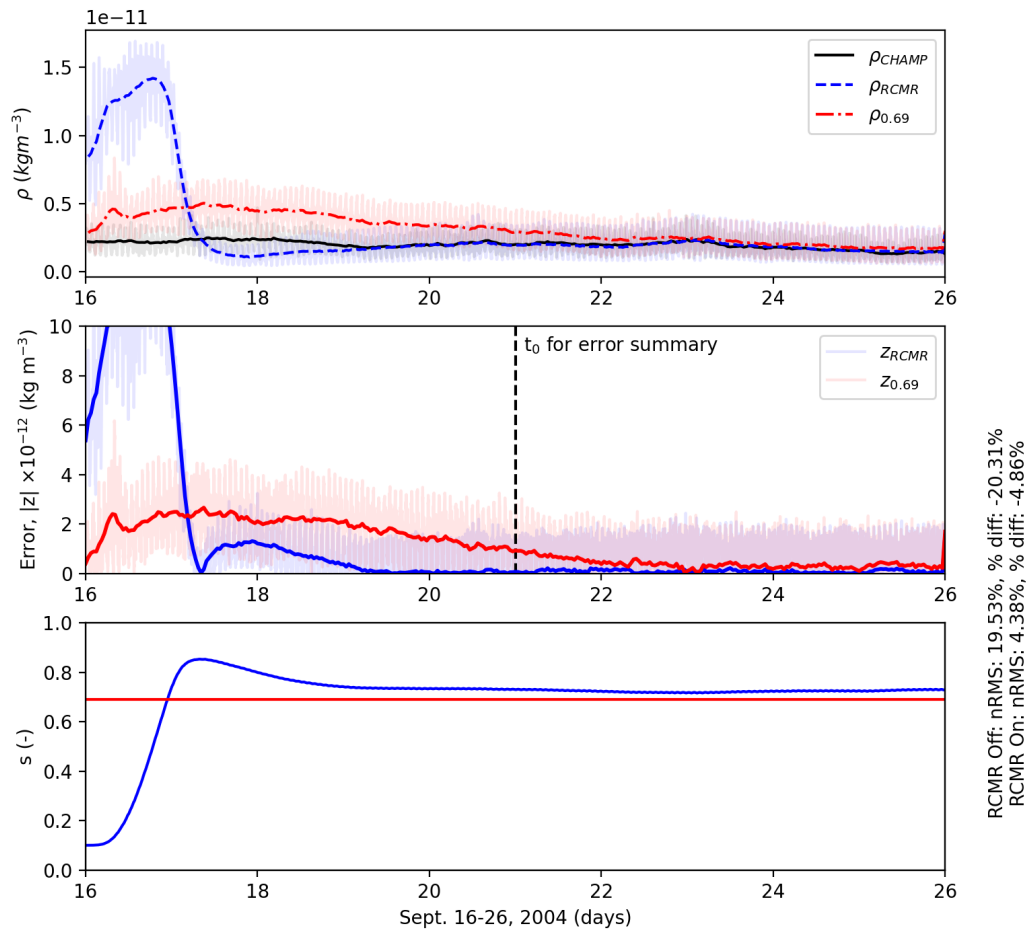
357 run. This set of thermal conductivity coefficients (4.6e-4, 4.6e-4, 0.69) matched the results
 358 found in the manual debiasing process.

359 Normalized root mean square (nRMS) and percent error are shown on the bottom
 360 right of Figures 7 and 8 to quantify the improvement with RCMR. These values were
 361 computed based on orbit-averaged densities for the final five days of the run (marked
 362 as t_0 on the figure). This gave sufficient time for RCMR to debias the model and allow
 363 GITM to reach a roughly diurnally reproducible state. In Figure 8, the nRMS and percent
 364 difference show improvement of $\pm 33\%$ percent error and nRMS to less than 3%.



365 **Figure 8.** Same as Figure 7, except using GRACE instead of CHAMP. The local time of ascending node
 366 for GRACE was 21.7 LT.

367 Switching to the time period in 2004, a similar simulation was performed using
368 CHAMP data to check the robustness of RCMR under different solar conditions. The
369 F10.7 was considerably lower for this run mostly being between 90-110 $\text{Wm}^{-2}\text{Hz}^{-1}$,
370 while the seasonality and geomagnetic activity was similar. Recall that debiasing between
371 September 2002 and 2004 was possible with similar thermal conductivity coefficients, and
372 so running this time period gave RCMR the opportunity to demonstrate this. As shown
373 in Figure 9, the RCMR and non-RCMR mass densities converged to CHAMP measure-
374 ments with RCMR reducing the time to converge by nearly seven days. In the bottom
375 subplot, the estimated thermal conductivity exponent converges to right around 0.70 which
376 is consistent with the RCMR test performed in 2002 and the manual debiased simula-
377 tions. nRMS and percent error were used to quantify the improvement with RCMR. They
378 showed a much larger improvement from a roughly -20% percent error and nRMS to less
379 than 5%.

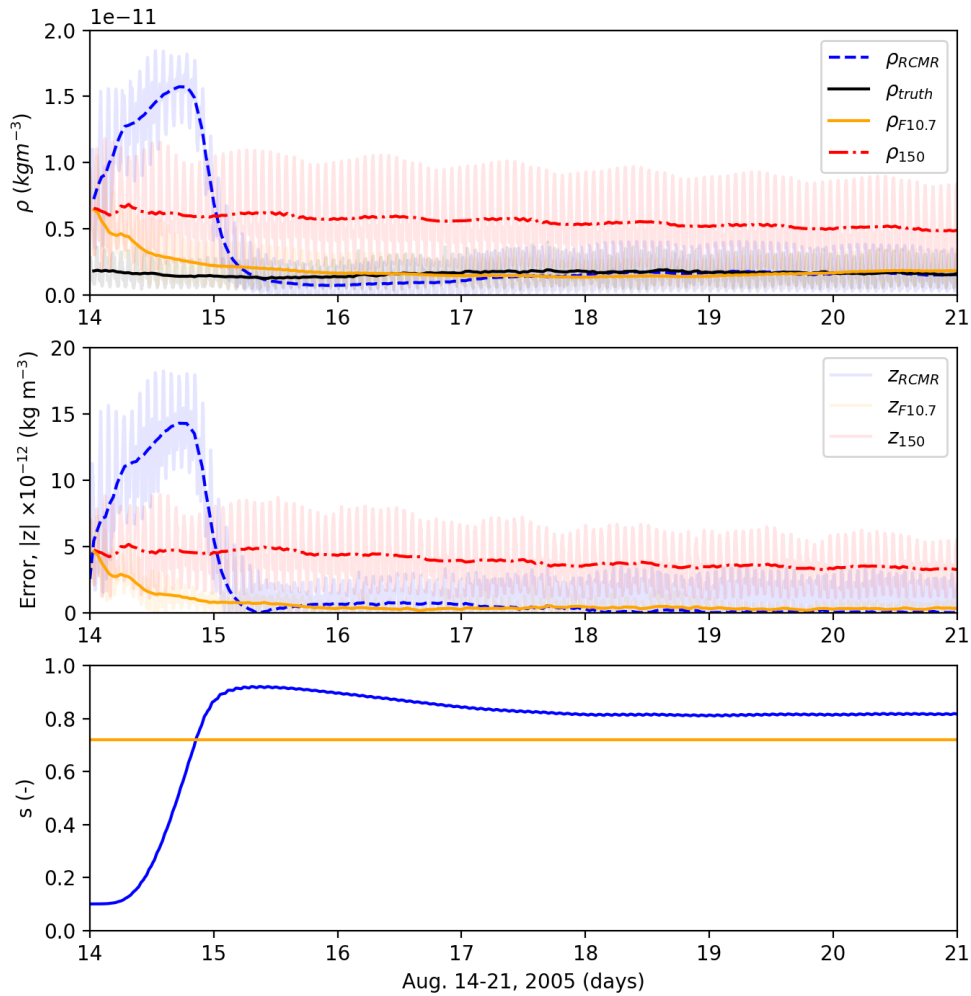


380 **Figure 9.** Same as Figure 7, except for September 2004. The local time of ascending node for CHAMP was
 381 19.4 LT.

382 **3.3 Storm-time Debiasing and Forecasting**

383 In this section, GITM was debiased by RCMR before the storm in August 2005.
 384 The F10.7 for this time period was lower than the previous runs shown. It varied between
 385 70-100 $\text{W m}^{-2}\text{Hz}^{-1}$. Comparisons between the typical GITM run, a purposefully biased
 386 GITM run, an RCMR-assisted GITM run with purposefully biased F10.7, and CHAMP
 387 data were made in an effort to improve forecasting of density enhancements during and
 388 after the storm.

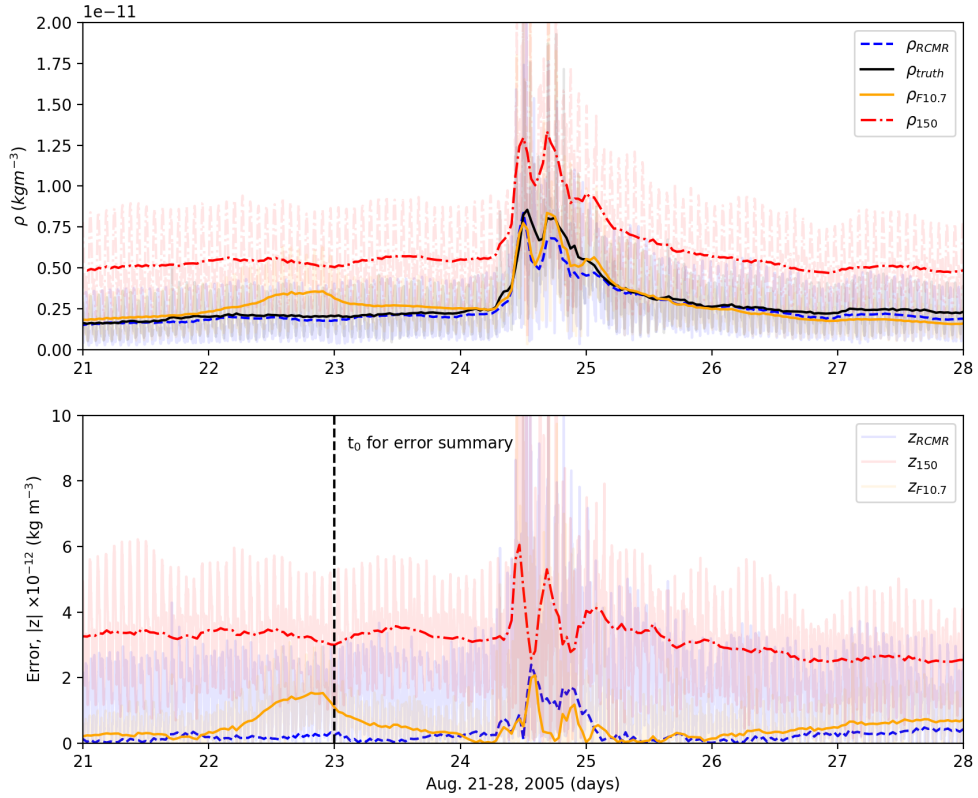
389 The storm took place between August 24-26, 2005. In the RCMR run, the debiasing
390 took place from August 14-21. The run continued through the storm from August 21-28
391 without the assistance of RCMR. During the storm, the exponent 's' was held constant
392 at its last value specified by RCMR on August 21. In Figure 10, the debiasing was done
393 prior to the storm using CHAMP measurements. As was done before, the densities, errors
394 and dynamic thermal conductivity exponent are shown in comparison to the static runs.



395 **Figure 10.** The densities and errors compared to CHAMP during August 2005 with RCMR on (blue) and
 396 RCMR off in two conditions. One run is with the daily averaged F10.7 values included (orange) and the other
 397 is with a constant, incorrect F10.7 of 150 (red). Both of the non-RCMR runs have the same constant thermal
 398 conductivity exponent, but only one of them is shown. The RCMR run is done with the incorrect F10.7. The
 399 bottom subplot shows the consequent thermal conductivity coefficient estimated.

400 As expected, the biased run with a constant F10.7 of $150 \text{ W m}^{-2} \text{ Hz}^{-1}$ was very dif-
 401 ferent than the CHAMP measurements and a GITM run using real F10.7 measurements. It
 402 is important to point out that the parameter estimation from RCMR showed that the best
 403 exponent s was around 0.8 which was considerably larger than the other runs. The F10.7

404 of $150 \text{ Wm}^{-2}\text{Hz}^{-1}$ is higher than the true conditions artificially increasing mass densities.
 405 To counteract this, an increased thermal conductivity was needed to dissipate this excess
 406 energy, reducing the mass density.



407 **Figure 11.** Similar to the previous figure, but for the August 21st-28th, 2005. RCMR is turned off so no
 408 thermal conductivities are being shown.

409 Figure 11 shows the runs proceeding through the storm and storm recovery. For
 410 the three days after RCMR was turned off, the densities stayed debiased. The storm was
 411 better represented because of this, although GITM with RCMR under predicted the storm
 412 response during the peaks. This is most likely due to the increased thermal conductivity,
 413 which pulled energy out of the thermosphere too quickly during the storms. This is rela-
 414 tively minor compared to the biased model results though. The RCMR run matched the
 415 recovery density after the storm quite well. Additional performance assessment metrics are
 416 shown in Table 4. The formulations for each metric is shown in *Kalafatoglu Eyiguler et al.*

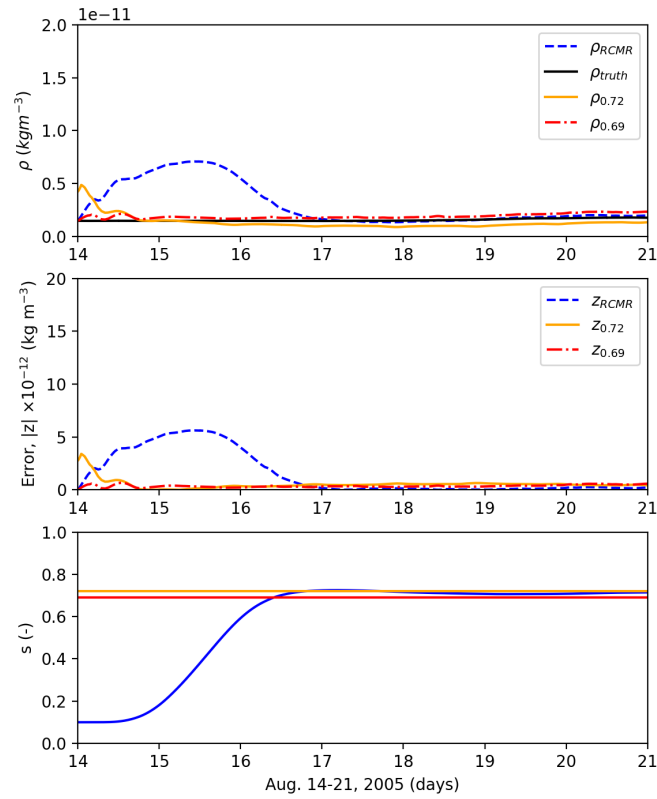
417 [2019]. When comparing the RCMR run to the biased run, the RCMR run performed
418 better in every metric. Each of these statistics help quantify the improvements that can be
419 had to the mean and variability of the mass densities.

420 On the other hand, the calibrated model of GITM also performed better than the
421 biased run. Comparing the RCMR run and the calibrated model of GITM, the Ratio_{avg} of
422 the default GITM simulation performed better than the RCMR run. RCMR was capable
423 of improving the time delay (TD) of the storm peak, the mean average error (MAE) and
424 normalized root mean square error (NRMSE).

425 **3.4 Debiasing using an Empirical Model**

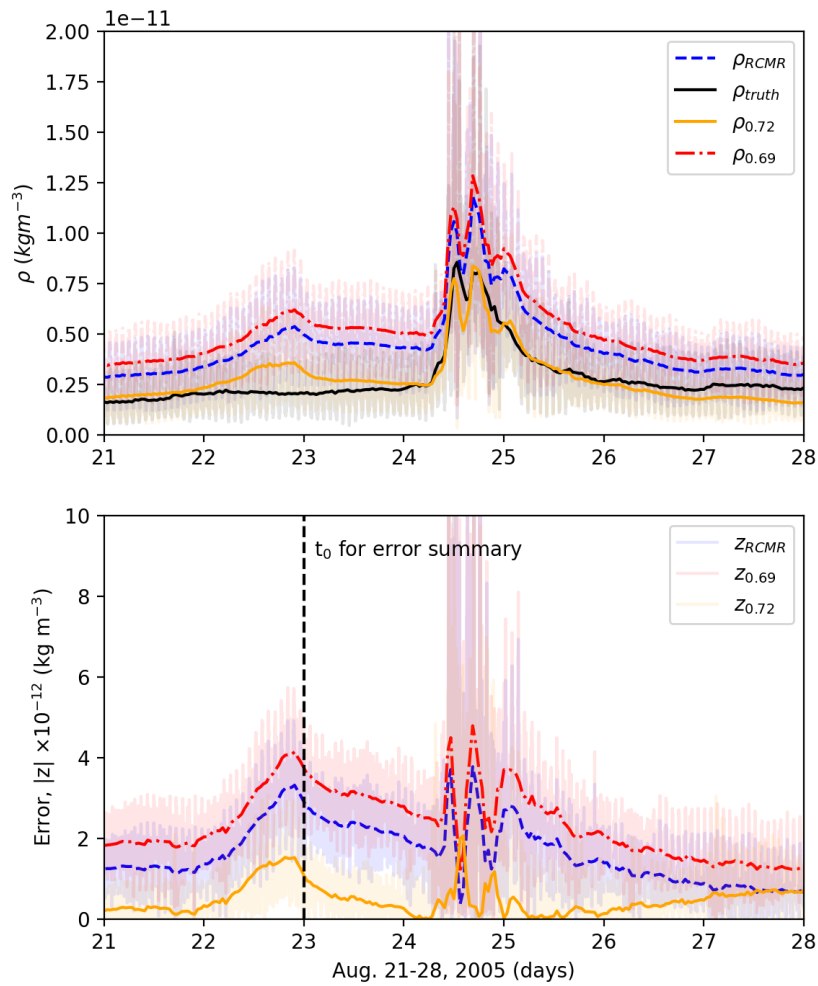
426 Satellite measurements of the thermosphere are not always available, especially
427 during real-time operations. For this reason, an empirical model such as MSIS may be
428 useful as a source of "truth data". Whereas empirical models are not always skilled at cor-
429 rectly predicting highly perturbed events, like solar storms, they are useful for obtaining
430 information on the background state. Further, satellite orbits may not be ideally placed
431 to represent the global conditions, while an empirical model can be sampled anywhere
432 (or everywhere). While satellite data is the ideal choice for debiasing, using an empirical
433 model may help in some situations. For these reasons, a final test was run to attempt to
434 debias GITM under conditions where satellite data was (in theory) not available.

439 In this run, MSIS mass densities at the subsolar point at 400 km altitude were used
440 as the source of "truth data". The same time period in August 2005 was used for this.
441 RCMR was allowed to debias GITM for seven days and then proceed through the storm.
442 During the storm, RCMR was turned off and the storm-time performance evaluation of
443 GITM was checked against CHAMP data, as in the previous case.



435 **Figure 12.** The densities and errors compared to MSIS at the 400 km altitude sub-solar point during August
 436 2005 with RCMR on (blue) and RCMR off in two conditions. One run is with manually calibrated thermal
 437 conductivity values included (orange) and the other is with a constant, biased thermal conductivity exponent
 438 of 0.69 (red). The bottom subplot shows the consequent thermal conductivity coefficient estimated.

445 In Figure 12 shows the mass density for different runs at the subsolar point at 400
 446 km altitude, which is where the MSIS data was extracted. The biased run (labeled $\rho_{0.69}$)
 447 and RCMR run no longer had error induced by the F10.7. The only source of error in the
 448 RCMR run (ρ_{RCMR}) was the initial value of 0.1 given to the thermal conductivity expo-
 449 nent s . The thermal conductivity exponent s in the wrong tuning run was 0.69, whereas
 450 the best tuning had an exponent of 0.72 ($\rho_{0.72}$). At the 400 km, subsolar point each run
 451 converged to MSIS results within a few days of the run. As shown in the bottom subplot,
 452 RCMR estimated the 's' to be 0.71, using the MSIS results.



444

Figure 13. Similar to Figure 11, but for the MSIS debris mass densities at CHAMP locations.

453

454

455

456

457

458

459

460

Figure 13 shows the same runs proceeding through the storm and storm recovery, but now at the CHAMP positions. These densities are quite different than the subsolar density, since CHAMP is a high inclination satellite sampling the high latitudes, where the energy balance can be quite different. In this case, the biased run performed worst of the three runs. In Table 4, the same performance tools from *Kalafatoglu Eyiguler et al.* [2019] are shown. The RCMR run performed similarly or better than the biased run, but considerably worse than the calibrated GITM run. This is due to the difference between MSIS and CHAMP during the preceding time period. Since RCMR was debiasing to-

Performance Assessment Tool	$\rho_{F10.7}$	ρ_{150}	ρ_{RCMR}	$\rho_{0.72}$	$\rho_{0.69}$	ρ_{RCMR}
Ratio _{max} (-)	0.98	1.56	0.98	0.98	1.5	1.38
Ratio _{avg} (-)	0.96	2.00	0.9	0.96	1.75	1.52
TD (hours)	3.8	3.8	-0.8	3.8	3.8	3.8
MAE (kg/m ³)	4.44e-13	3.13e-12	3.47e-13	4.44e-13	2.35e-12	1.64e-12
NRMSE (%)	8.32	48.68	8.29	8.32	38.15	27.41
PE (-)	0.65	-1.06	0.65	0.65	-0.62	-0.16

466 **Table 4.** Statistical analysis on orbit-averaged data from t_0 for each run in Figure 11. The first two are di-
467 mensionless quantities. TD is the time difference between storm peak as seen from data and from the model
468 computed in hours. The mean average error (MAE) has units of kg/m³. The normalized root mean square
469 error (NRMSE) is shown as a percentage. The prediction efficiency (PE) is also a non-dimensional statistic.
470 The columns are separated by run-type the first three columns being associated with debiasing with CHAMP
471 data and the final three columns are associated with debiasing with MSIS.

461 wards MSIS, the debiasing improvement is subject to the accuracy of MSIS. It is possible
462 that debiasing with MSIS at locations other than at 400 km altitude at the subsolar point
463 could improve this, but it was not explored in this work. This simulation does show that
464 debiasing with an empirical model improves the performance of the biased model, but
465 then is subject to other limitations.

472 **4 Summary and Conclusion**

473 In this work, GITM used RCMR with CHAMP and GRACE satellite measurements
474 to correct for uncertain parameters and incorrect drivers. During these runs, it was shown
475 that after sufficient error accumulation, RCMR was able to reduce the bulk of the error
476 and nRMS to below 5% within 2-3 days. This work also showed the effectiveness of de-
477 biasing GITM prior to a storm in August 2005 with CHAMP measurements and MSIS.
478 When debiasing was applied before a storm, the results during the storm were shown
479 to improve in all metrics except the time delay between a measured storm peak and the
480 model-predicted peak (where they performed identically with and without RCMR). It was

481 demonstrated that RCMR could use empirical models within GITM to debias the model,
482 but this was reliant on MSIS results having low error during the pre-storm time period
483 and the choice of where to sample the empirical model. Future work will show more
484 runs and have a statistical approach to address how beneficial using MSIS for parameter
485 estimation can be.

486 **Acknowledgments**

487 The research presented in this study was supported at University of Michigan partially by
488 the U.S. Air Force Office of Scientific Research under Dynamic Data-Driven Applications
489 Systems grant FA9550-16-1-0071. This work was also supported by the joint NSF-NASA
490 Space Weather with Quantified Uncertainties program under NSF grant number 2028125
491 and NASA grant number 80NSSC20K1581. GITM is freely available through GitHub
492 (<https://github.com/aaronjridley/GITM>). Dst obtained from the World Data Center in Ky-
493 oto, Japan (<https://wdc.kugi.kyoto-u.ac.jp/dst/dir/>). CHAMP and GRACE satellite data is
494 available through Technical University, Delft (<http://thermosphere.tudelft.nl/>).

495 **References**

- 496 Banks, P. M., and G. Kockarts (1973), *Aeronomy*, 372 pp., Academic Press, doi:
 497 10.1016/C2013-0-10329-7.
- 498 Barlier, F., C. Berger, J. Falin, G. Kockarts, and G. Thuillier (1969), *Aeronomica acta*,
 499 *Inst. Aéronomie Spatiale, Bruxelles*.
- 500 Bell, J. M., S. W. Bougher, J. H. Waite Jr., A. J. Ridley, B. A. Magee, K. E. Mandt,
 501 J. Westlake, A. D. DeJong, A. Bar–Nun, R. Jacovi, G. Toth, and V. De La Haye (2010),
 502 Simulating the one-dimensional structure of titan’s upper atmosphere: 1. formulation of
 503 the titan global ionosphere-thermosphere model and benchmark simulations, *Journal of*
 504 *Geophysical Research: Planets*, 115(E12), doi:10.1029/2010JE003636.
- 505 Bougher, S. W., D. Pawlowski, J. M. Bell, S. Nelli, T. McDunn, J. R. Murphy, M. Chizek,
 506 and A. Ridley (2015), Mars global ionosphere-thermosphere model: Solar cycle, sea-
 507 sonal, and diurnal variations of the mars upper atmosphere, *Journal of Geophysical*
 508 *Research: Planets*, 120(2), 311–342, doi:10.1002/2014JE004715.
- 509 Bowman, B., W. Tobiska, and F. Marcos (2006), A new empirical thermospheric density
 510 model jb2006 using new solar indices, in *AIAA/AAS Astrodynamics Specialist Confer-*
 511 *ence and Exhibit*, p. 6166.
- 512 Bowman, B., W. K. Tobiska, F. Marcos, C. Huang, C. Lin, and W. Burke (2008), *A New*
 513 *Empirical Thermospheric Density Model JB2008 Using New Solar and Geomagnetic*
 514 *Indices*, doi:10.2514/6.2008-6438.
- 515 Bowman, B. R. (2004), The semiannual thermospheric density variation from 1970 to
 516 2002 between 200-1100 km, *Advances in the Astronautical Sciences*, 119, 04–174.
- 517 Brandt, D. A., C. D. Bussy-Virat, and A. J. Ridley (2020), A simple method for correct-
 518 ing empirical model densities during geomagnetic storms using satellite orbit data,
 519 *Space Weather*, 18(12), e2020SW002565, doi:https://doi.org/10.1029/2020SW002565,
 520 e2020SW002565 10.1029/2020SW002565.
- 521 Bruinsma, S., D. Tamagnan, and R. Biancale (2004), Atmospheric densities derived from
 522 CHAMP/STAR accelerometer observations, *Planetary and Space Science*, 52, 297–312,
 523 doi:10.1016/j.pss.2003.11.004.
- 524 Burrell, A., A. Goel, A. J. Ridley, and D. S. Bernstein (2015), Correction of the photo-
 525 electron heating efficiency within the global ionosphere-thermosphere model using ret-
 526 rospective cost model refinement, *Journal of Atmospheric and Solar-Terrestrial Physics*,
 527 124, doi:10.1016/j.jastp.2015.01.004.

- 528 Bussy-Virat, C. D., A. J. Ridley, and J. W. Getchius (2018), Effects of uncertainties in
529 the atmospheric density on the probability of collision between space objects, *Space*
530 *Weather*, *16*(5), 519–537, doi:<https://doi.org/10.1029/2017SW001705>.
- 531 Chamberlin, P. C., T. N. Woods, and F. G. Eparvier (2008), Flare irradiance spectral
532 model (fism): Flare component algorithms and results, *Space Weather*, *6*(5), doi:
533 10.1029/2007SW000372.
- 534 Chamberlin, P. C., F. G. Eparvier, V. Knoer, H. Leise, A. Pankratz, M. Snow, B. Tem-
535 pleman, E. M. B. Thiemann, D. L. Woodraska, and T. N. Woods (2020), The flare
536 irradiance spectral model-version 2 (fism2), *Space Weather*, *18*(12), e2020SW002588,
537 doi:<https://doi.org/10.1029/2020SW002588>, e2020SW002588 10.1029/2020SW002588.
- 538 Doornbos, E., H. Klinkrad, and P. Visser (2008), Use of two-line element data for ther-
539 mosphere neutral density model calibration, *Advances in Space Research*, *41*(7), 1115–
540 1122, doi:<https://doi.org/10.1016/j.asr.2006.12.025>.
- 541 D’Amato, A. M., A. A. Ali, A. Ridley, and D. S. Bernstein (2013), Retrospective cost
542 optimization for adaptive state estimation, input estimation, and model refinement, *Pro-*
543 *cedia Computer Science*, *18*, 1919–1928, doi:<https://doi.org/10.1016/j.procs.2013.05.361>,
544 2013 International Conference on Computational Science.
- 545 Fuller-Rowell, T. J., and D. Rees (1980), A three-dimensional, time-dependent, global
546 model of the thermosphere, *Journal of the Atmospheric Sciences*, *37*.
- 547 Garcia, M. (2021), Space debris and human spacecraft.
- 548 Goel, A., A. J. Ridley, and D. S. Bernstein (2018), Estimation of the eddy diffusion co-
549 efficient using total electron content data, *2018 Annual American Control Conference*
550 *(ACC)*, doi:10.23919/ACC.2018.8431184.
- 551 Goel, A., B. M. Ponder, A. J. Ridley, and D. S. Bernstein (2020), Estimation of thermal-
552 conductivity coefficients in the global ionosphere–thermosphere model, *Journal of*
553 *Aerospace Information Systems*, *17*(9), 546–553, doi:10.2514/1.1010819.
- 554 Hedin, A. E. (1983), A revised thermospheric model based on mass spectrometer and
555 incoherent scatter data: Msis-83, *Journal of Geophysical Research: Space Physics*, *88*.
- 556 Hedin, A. E. (1987), Msis-86 thermospheric model, *Journal of Geophysical Research:*
557 *Space Physics*, *92*(A5), 4649–4662, doi:<https://doi.org/10.1029/JA092iA05p04649>.
- 558 Hedin, A. E. (1991), Extension of the msis thermosphere model into the middle and lower
559 atmosphere, *Journal of Geophysical Research: Space Physics*, *96*(A2), 1159–1172,
560 doi:<https://doi.org/10.1029/90JA02125>.

- 561 Hejduk, M. D., and R. K. Frigm (2015), Collision avoidance short course - part i: Theory.
- 562 Hilsenrath, J. e. a. (1960), Tables of thermodynamic and transport properties, *Pergamon*
- 563 *Press*.
- 564 Jacchia, L. G. (1970), New Static Models of the Thermosphere and Exosphere with Em-
- 565 pirical Temperature Profiles, *SAO Special Report*, 313.
- 566 Kalafatoglu Eyiguler, E. C., J. S. Shim, M. M. Kuznetsova, Z. Kaymaz, B. R. Bow-
- 567 man, M. V. Codrescu, S. C. Solomon, T. J. Fuller-Rowell, A. J. Ridley, P. M. Mehta,
- 568 and E. K. Sutton (2019), Quantifying the storm time thermospheric neutral den-
- 569 sity variations using model and observations, *Space Weather*, 17(2), 269–284, doi:
- 570 <https://doi.org/10.1029/2018SW002033>.
- 571 Kuang, D., S. Desai, A. Sibthorpe, and X. Pi (2014), Measuring atmospheric density using
- 572 gps-leo tracking data, *Advances in Space Research*, (53), 243–256.
- 573 Lide, E.-i. C., D. R. (1997), Crc handbook of chemistry and physics, *Boca Raton, FL:*
- 574 *CRC Press*.
- 575 Malhotra, G., A. J. Ridley, D. R. Marsh, C. Wu, and L. J. Paxton (2017), Understanding
- 576 the Effects of Lower Boundary Conditions and Eddy Diffusion on the Ionosphere-
- 577 Thermosphere System, in *AGU Fall Meeting Abstracts*, vol. 2017, pp. SA33A–2593.
- 578 Marcos, F. A. (1990), Accuracy of atmospheric drag models at low satellite altitudes,
- 579 *Advances in Space Research*, 10(3-4), 417–422.
- 580 Masutti, D., G. March, A. J. Ridley, and J. Thoemel (2016), Effect of the solar activity
- 581 variation on the global ionosphere thermosphere model (gitm), *Annales Geophysicae*,
- 582 34(9), 725–736, doi:10.5194/angeo-34-725-2016.
- 583 Moorthy, A. K., J. J. Blandino, M. A. Demetriou, and N. A. Gatsonis (2021), Extended
- 584 lifetime of cubesats in the lower thermosphere with active attitude control, *Journal of*
- 585 *Spacecraft and Rockets*, 58(6), 1876–1892, doi:10.2514/1.A34975.
- 586 Morozov, A., A. Ali, A. D’Amato, A. Ridley, S. Kukreja, and D. Bernstein (2011),
- 587 Retrospective-cost-based model refinement for system emulation and subsystem identi-
- 588 fication, *Proceedings of the IEEE Conference on Decision and Control*, pp. 2142–2147,
- 589 doi:10.1109/CDC.2011.6161284.
- 590 Pachura, D., and M. D. Hejduk (2016), Conjunction assessment late-notice high-interest
- 591 event investigation: Space weather aspects, *NASA Technical Reports Server*.
- 592 Pavlov, A. V. (2017), Thermal conductivity of the multicomponent neutral atmosphere,
- 593 *Journal of Geophysical Research: Space Physics*, 122(12), 12,476–12,485, doi:

594 10.1002/2017JA024397.

595 Pawlowski, D. J., and A. J. Ridley (2009), The effect of the characteristics of solar flares
596 on the thermospheric response, *AGU Fall Meeting Abstracts*, SA51A-1213.

597 Picone, J. M., A. E. Hedin, D. P. Drob, and A. C. Aikin (2002), Nrlmsise-00 empir-
598 ical model of the atmosphere: Statistical comparisons and scientific issues, *Jour-
599 nal of Geophysical Research: Space Physics*, 107(A12), SIA 15–1–SIA 15–16, doi:
600 10.1029/2002JA009430.

601 Qian, L., S. C. Solomon, and T. J. Kane (2009), Seasonal variation of thermospheric
602 density and composition, *Journal of Geophysical Research: Space Physics*, 114(A1),
603 doi:https://doi.org/10.1029/2008JA013643.

604 Reid, R., J. Prausnitz, and T. K. Sherwood (1977), The properties of gases and liquids,
605 *New York: McGraw-Hill Book Co.*

606 Richards, P. G., J. A. Fennelly, and D. G. Torr (1994), Euvac: A solar euv flux model
607 for aeronomic calculations, *Journal of Geophysical Research: Space Physics*, 99(A5),
608 8981–8992, doi:https://doi.org/10.1029/94JA00518.

609 Richmond, A. D., E. C. Ridley, and R. Roble (1992), A thermosphere/ionosphere general
610 circulation model with coupled electrodynamics, *Geophys. Res. Lett.*, 19.

611 Ridley, A. J., Y. Deng, and G. Tóth (2006), The global ionosphere-thermosphere model,
612 *Journal of Atmospheric and Solar-Terrestrial Physics*, 68, 839–864.

613 Saleh, J. H., D. E. Hastings, and D. J. Newman (2004), Weaving time into system archi-
614 tecture: satellite cost per operational day and optimal design lifetime, *Acta Astronautica*,
615 54(6), 413 – 431, doi:https://doi.org/10.1016/S0094-5765(03)00161-9.

616 Santillo, M. A., and D. S. Bernstein (2010), Adaptive control based on retrospective
617 cost optimization, *Journal of Guidance, Control, and Dynamics*, 33(2), 289–304, doi:
618 10.2514/1.46741.

619 Schunk, R. W., and A. F. Nagy (2004), *Ionospheres*, 570 pp., Cambridge University Press.

620 Storz, M. F., B. R. Bowman, M. J. I. Branson, S. J. Casali, and W. K. Tobiska (2005),
621 High accuracy satellite drag model (hasdm), *Advances in Space Research*, 36(12), 2497
622 – 2505, doi:https://doi.org/10.1016/j.asr.2004.02.020, space Weather.

623 Vargaftik, N. B., L. P. Filippov, A. A. Tarzimanov, and E. E. Totskii (1993), *Handbook of
624 Thermal Conductivity of Liquids and Gases*, 368 pp., CRC Press.

625 Wang, X., J. Miao, X. Lu, E. Aa, B. Luo, J. Liu, Y. Hong, Y. Wang, T. Ren, R. Zeng,
626 C. Du, and S. Liu (2022), Using temporal relationship of thermospheric density

627 with geomagnetic activity indices and joule heating as calibration for nrlmsise-
628 00 during geomagnetic storms, *Space Weather*, 20(4), e2021SW003017, doi:
629 <https://doi.org/10.1029/2021SW003017>, e2021SW003017 2021SW003017.